Article

Exploring Electrochemical Sensing for Fungicide Detection: Utilization of Newly Synthesized Oligomers

Veeramani Mangala Gowri, Pontagarn Chanpuang, Warit Bunrueang, Tanawat Imboon, Dusadee Khamboonrueang, Chaisak Issro, Mutsuhiro Shima, and Sirikanjana Thongmee*

Read Online

ACCESS		Metrics & More		Article Recommendations		Supporting Information

AMTa-3-amino-5-mercapto-1,2,4-triazole ; HAuCl₄-hydrogen tetrachloroaurate (III); TBZ-thiabendazole; H₂SO₄-sulfuric acid; GC-glassy carbon electrode; RF-reference electrode; CE-counter electrode; ● - Oligo AMTa.
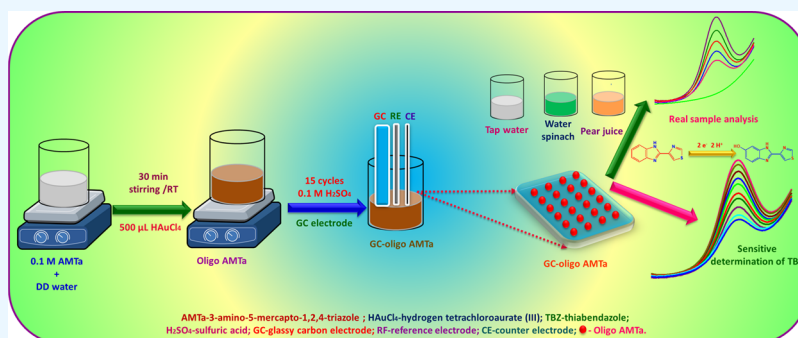
ABSTRACT: The determination of thiabendazole is crucial for ensuring food safety, environmental protection, and compliance with regulatory standards. Accurate detection helps prevent harmful exposure, ensuring the safety of agricultural products and safeguarding public health. Therefore, this study investigates the electrochemical sensing capabilities of newly synthesized oligo 3-amino-5-mercapto-1,2,4-triazole (oligo AMTa) using hydrogen tetrachloroaurate (III) (HAuCl₄) as an oxidizing agent at room temperature for thiabendazole (TBZ) detection, employing a simple electrode fabrication process. The prepared oligo AMTa was thoroughly characterized using UV−visible spectroscopy, scanning electron microscopy (SEM), Energy Dispersive X-ray Analysis (EDAX), X-ray diffraction (XRD), X-ray photoelectron spectroscopy (XPS), high-resolution mass spectroscopy (HR-MS), and Fourier-transform infrared spectroscopy (FT-IR) to confirm its oligomerization structure and properties. The IR spectrum of oligo AMTa reveals a new peak at 1449 cm⁻¹, indicating the conversion of −NH₂ groups to −N═N− groups during oligomerization, unlike AMTa. Additionally, the disappearance of the −SH group peak at 2615 cm⁻¹ in oligo AMTa suggests an S−S linkage involvement in the oligomerization process. In the oligo AMTa XPS spectrum, the presence of C═N is displayed by a small peak at 287.3 eV, and oligomerization via −NH and N═N is confirmed by the lack of a 284.0 eV peak for C−C or C═C. Gold nanoparticle formation is not demonstrated by the 84.8 eV peak, which implies that the gold atom is not in the Au⁰ state. The HR-MS spectrum of oligo AMTa shows a peak at m/z 564.08, indicating a chain of five monomers, and another peak at m/z 435.03, confirming the presence of a tetrameric form of AMTa. After that, the GC electrode was directly linked to the oligo AMTa by the potentiodynamic method. SEM, electrochemical impedance spectroscopy (EIS), and cyclic voltammetry (CV) were all employed to confirm the fabrication of oligo AMTa. The SEM image illustrates the formation of a particlelike structure with a uniform size of the oligomer after cycling in 0.1 M H₂SO₄. After electrocycling, the size of the oligomer was reduced from 2.6 μm to 30 nm. The oligo AMTa-modified electrode possesses the highest electroactive surface area and electrical conductivity due to several key factors. First, the presence of amino (−NH₂) and thiol (−SH) functional groups in AMTa enhances the surface coverage and density of electroactive sites, increasing the electroactive surface area. Additionally, the conjugated structure of AMTa facilitates efficient electron transfer, resulting in enhanced electrical conductivity compared to unmodified electrodes. Eventually, the electrochemical oxidation of TBZ occurred using the fabricated electrodes. The GC/oligo AMTa electrode exhibited a four-fold increase in oxidation current for TBZ compared to unmodified GC electrodes. This enhancement is due to the improved surface properties from the oligo

continued...

AMTa modification, which significantly boosts TBZ adsorption through strong interactions like hydrogen bonding and $\pi-\pi$ stacking. These interactions, along with the increased surface area and catalytic properties, facilitate effective electron transfer, resulting in a higher oxidation current. As an outcome, the film was employed to determine the sensitivity level of TBZ, and a LOD of 1.8×10^{-11} M (S/N = 3) was found. The straightforward method's practical utility was proven by measuring TBZ in tap water, water spinach, and pear juice samples. The comprehensive characterization of oligo AMTa provided insights into its interaction mechanisms with thiabendazole, contributing to the development of a reliable, cost-effective, and efficient sensor.

1. INTRODUCTION

Chemical polymerization is a fundamental process in materials science and chemistry that involves the transformation of small molecules called monomers into large, chain-like molecules known as polymers. These polymers are integral to a vast array of applications, spanning everyday products such as plastics and textiles to advanced uses in medicine, electronics, and aerospace engineering.[1−4] Chemical and electrochemical polymerization are two distinct methods used to synthesize polymers, each with unique mechanisms and applications. Electrochemical polymerization, on the other hand, utilizes an applied electrical potential to induce polymerization, often resulting in the formation of conductive polymers. This technique is particularly effective for in situ polymerization on electrode surfaces, making it valuable for creating thin films and coatings in electronic applications.[2,5−8] Chemical polymerization involves the use of chemical initiators or catalysts to start the polymerization process, which can occur via various mechanisms such as free radical, ionic, or coordination polymerization. This method is highly versatile and can produce a wide range of polymers with controlled molecular weights and structures. Chemical polymerization offers several advantages over electrochemical polymerization.[9−15] First, chemical polymerization is highly versatile, accommodating a broad spectrum of monomers and allowing for the synthesis of diverse polymers with tailored properties. This versatility is particularly important for producing materials with the specific mechanical, thermal, and chemical characteristics required for various industrial applications. Second, chemical polymerization methods provide superior control over molecular weight and polymer architecture, which is crucial for achieving the desired performance in the final polymer product. This precise control is less attainable in electrochemical polymerization due to the complexities of the electrochemical environment. Additionally, chemical polymerization processes are generally more scalable and economically viable for large-scale production. They do not require the specialized equipment and stringent conditions needed for electrochemical polymerization, making them more accessible for widespread industrial use. Overall, the flexibility, control, and scalability of chemical polymerization make it a preferred method for producing a wide array of polymeric materials.[9−15] For example, Zhang et al. developed an in situ amplified electronic monitoring system to detect lead ions. The system utilizes a Pb^{2+}-dependent DNAzyme for signal amplification, employing a hybridization chain reaction for DNA self-assembly. Signal detection is enhanced through DNAzyme-catalyzed polymerization of aniline, ensuring sensitive and selective detection of lead ions.[11] Chen et al. utilized polyvinylpyrrolidone (PVP) to modify Pt nanoclusters (Pt NCs), creating water-stable nanozymes with enhanced peroxidase-mimicking activity (up to 16.3 U/mg). This enhancement stemmed from surface ligand modifications and electron-absorbing effects on the Pt NCs. Density functional theory revealed lower OH-transition potentials for the PVP-modified Pt NCs. Their optimized

nanozyme immunoassay demonstrated an ultrawide dynamic range (0.005−50 ng/mL) for cardiac troponin I detection, achieving a remarkable detection limit of 1.3 pg/mL. This approach sets a pathway for designing highly active artificial enzymes, expanding the scope of enzyme alternatives in practical applications.[13]

Intrinsically conducting polymers (ICPs), particularly heterocyclic polymers such as polyaniline, polypyrrole, and polythiophene, have been extensively investigated for decades. ICPs possess a unique combination of electrical conductivity and the advantageous properties of conventional polymers such as flexibility, processability, and chemical resistance. This distinct blend of features provides several key advantages.[9−23] First, their electrical conductivity, which can be tuned through chemical doping, allows ICPs to be used in a variety of electronic applications, including organic light-emitting diodes (OLEDs), organic photovoltaics (OPVs), and field-effect transistors (FETs). Second, their mechanical flexibility and lightweight nature make them ideal for use in flexible and wearable electronic devices, where traditional rigid materials would be impractical. As an illustration, Cu_xO-polypyrrole conductive aerogel loaded on a graphene oxide framework (CuxO-PPy@ GO) was used to detect H_2S on a flexible paper substrate with outstanding performance. With LED illumination and image processing, this 3D porous design allows signal detection on a smartphone through a self-referenced imaging platform.[20] Susceptible room-temperature H_2S gas sensors were introduced by Tang and co-workers using Cu^{2+} doped SnO_2 nanograin/ poly pyrrole nanospheres. Compared to pristine SnO_2 nanograins, the organic−inorganic nanohybrids considerably improve response and recovery rates, enhancing the sensitivity seven times. This suggests broader implications in functional material design and potential real-time H_2S monitoring.[21] Third, the processability of ICPs via methods such as solution casting, printing, and coating enables the fabrication of complex and large-area devices with relative ease, significantly reducing production costs.[9−23] Additionally, ICPs can exhibit excellent environmental stability and can be engineered to withstand various physical and chemical conditions, enhancing their durability and lifespan in real-world applications. Furthermore, the biocompatibility of certain ICPs opens up innovative uses in biomedical devices such as biosensors and drug delivery systems. For example, Zeng et al. developed a novel biosensing platform using polyaniline nanowires-functionalized reduced graphene oxide (PANI/rGO) for Kanamycin detection, enhanced by platinum nanozyme-catalyzed gas generation. Signal amplification was achieved through catalytic hairpin assembly (CHA) and strand-displacement amplification (SDA), showcasing a versatile approach for sensitive biosensing applications.[19] Overall, the multifunctionality and adaptability of ICPs position them as vital materials in creating efficient, flexible, and durable photochemical and electrochemical devices.[9−23]

ICPs including polyaniline, polypyrrole, polythiophene, poly(ethylenedioxythiophene), 2-Aminothiazole (2-AT), 2-amino-1,3,4-thiadiazole (ATD), 3-amino-1,2,4-triazole (ATA),

2-aminobenzothiazole (2-ABT), poly-2-mercapto-1,3,4-thiadia-zole (PTT), poly-2,5-dimercapto-1,3,4-thiadiazole (DMTD), 5-amino-1,3,4-thiadiazole-2-thiol (AMT) and 3-amino-5-mercap-to-1,2,4-triazole (AMTa)[5−38] have been chemically and electro-chemically synthesized so far. ICPs have been studied broadly for the development of biosensors and are well-known for their suitability with biological molecules in neutral aqueous solutions.[5−38] Also, conducting polymers efficiently transfer the electric charges produced by biochemical reactions to electronic circuits. Therefore, ICPs may be used as immobilizing matrices for biomolecules and provide a suitable environment for their immobilization.[5−38] The electrochemical polymer-ization of AMTa has been explored, similar to other heterocyclic conducting polymers/oligomers.[38] As of yet, there has been no reported chemical oxidative polymerization of AMTa. There is significant interest in constructing materials with interesting properties using AMTa due to its unique chemical structure and versatile reactivity. AMTa, a heterocyclic compound containing both amino and mercapto groups, offers a rich array of functional groups for chemical modification, making it a valuable building block for the synthesis of diverse materials. One area of interest lies in utilizing AMTa as a ligand for coordination chemistry, where its sulfur and nitrogen atoms can coordinate with transition metals to form coordination complexes with intriguing electronic and magnetic properties. Additionally, AMTa's ability to undergo polymerization/oligomerization reactions makes it a promising monomer for the fabrication of conjugated polymers/oligomers with tailored electrical and optical properties. Furthermore, the presence of both amino and mercapto groups in AMTa offers the potential for constructing multifunctional materials with applications in catalysis, sensing, drug delivery, and biomedicine. Overall, the unique structural features and versatile reactivity of AMTa make it an attractive candidate for the design and synthesis of materials with a wide range of interesting properties and applications. The current investigation thus describes the chemical oxidative oligomerization of AMTa (oligo AMTa) and investigates their optical, electrochemical, and morphological properties.

Determining thiabendazole, a widely used fungicide and anthelmintic, in real samples such as agricultural products, water, and biological fluids is crucial for ensuring food safety, environmental protection, and compliance with regulatory standards.[39−46] In addition to electrochemical methods, several other analytical techniques are available for determining thiabendazole concentrations in various matrices. High-performance liquid chromatography (HPLC) is a widely used method known for its high accuracy and ability to separate thiabendazole from complex sample matrices. HPLC is often coupled with UV or fluorescence detection to enhance sensitivity. Gas chromatography (GC), particularly when coupled with mass spectrometry (GC-MS), provides excellent sensitivity and specificity, making it suitable for trace analysis of thiabendazole.[39−46] Spectrophotometric methods, including UV−vis and fluorescence spectroscopy, offer simpler and cost-effective alternatives but typically require derivatization or preconcentration steps to achieve adequate sensitivity. Addi-tionally, immunoassay techniques, such as enzyme-linked immunosorbent assays (ELISA), provide high specificity and are useful for screening large numbers of samples, although they may be less quantitative compared to chromatographic methods.[39−46] Overall, the choice of method depends on factors, such as the required sensitivity, specificity, available instrumentation, and the nature of the sample matrix.

The electrochemical method offers several advantages for determining the thiabendazole content in real samples. First, electrochemical techniques provide high sensitivity and selectivity, allowing for the detection of thiabendazole at low concentrations in complex matrices such as agricultural products, water, and biological fluids.[46−52] This high sensitivity enables accurate quantification, even in samples with trace amounts of the analyte, ensuring compliance with regulatory limits and enhancing food safety and environmental monitoring efforts. Second, electrochemical methods offer rapid analysis times, enabling real-time or near-real-time monitoring of thiabendazole levels.[46−52] This rapid response is particularly valuable for on-site analysis and process control applications, where the timely detection of contaminants is critical for ensuring product quality and safety. Additionally, electro-chemical sensors can be easily miniaturized and integrated into portable devices, enabling field measurements and on-site screening without the need for extensive sample preparation or specialized laboratory equipment. This portability and ease of use make electrochemical methods highly accessible and applicable in a wide range of settings, from agricultural fields to industrial facilities, enhancing the efficiency and effectiveness of thiabendazole determination in real-world scenarios.[46−52]

The aim of this research is to establish a first-time report on the synthesis of an oligomer with AMTa as the monomer and hydrogen tetrachloroaurate (III) (HAuCl$_4$) as the oxidizing agent at room temperature. The resulting oligo AMTa was subsequently evaluated for its electrocatalytic activity to oxidize TBZ on glassy carbon (GC) electrodes. According to our lab publications, AMTa's electropolymerized film has remarkable electrocatalytic properties, which is why we selected it as a monomer. Reports about the oligomerization process using AMTa as the monomer are nonexistent. HAuCl$_4$ was used as an oxidizing agent in this oligomerization process, oxidizing the monomer to the oligomer. For several months, the resultant oligo AMTa remained quite stable. The oligo AMTa was assembled on the GC electrode by the simple potentiodynamic method. UV−visible spectroscopy, XRD, FT-IR, XPS, SEM, and HR-TEM studies were used to characterize the development of oligomers. The fabricated electrode was subsequently effectively utilized for TBZ monitoring. An assessment of the TBZ concentration in tap water, pear juice, and water spinach samples demonstrated the practical implications of the oligo AMTa-modified electrode.

2. EXPERIMENTAL SECTION

2.1. Materials and Methods. The following materials were utilized in this study: Glassy carbon (GC) plates, sodium dihydrogen phosphate dihydrate, disodium hydrogen phosphate dihydrate, 3-amino-5-mercapto-1,2,4-triazole (AMTa), hydro-gen tetrachloroaurate (III) (HAuCl$_4$), N-Methyl-2-pyrrolidone (NMP) and thiabendazole (TBZ). Further, EDAX, FT-IR, HR-TEM, UV−visible spectrophotometer, XRD, XPS, SEM, EDAX, and HR-TEM techniques have been utilized to characterize the materials. Electrochemical experiments such as CV, EIS, DPV, and amperometry were carried out in a standard three-electrode cell utilizing a CHI electrochemical analyzer. The specific materials and instrumentation procedures were included in the section that provided Supporting Information.

2.2. Synthesis of Oligo AMTa by Chemical Method. In 35 mL of DD water, 400 μL of the 0.01 M AMTa aqueous solution was dissolved to produce oligo AMTa. The mixture was agitated for 30 min at ambient temperature. Following that, the

Scheme 1. (A) Preparation of Oligo AMTa by the Wet Chemical Method at Ambient Temperature and (B) Fabrication of Oligo AMTa on the GC Electrode Surface by the Potentiodynamic Method
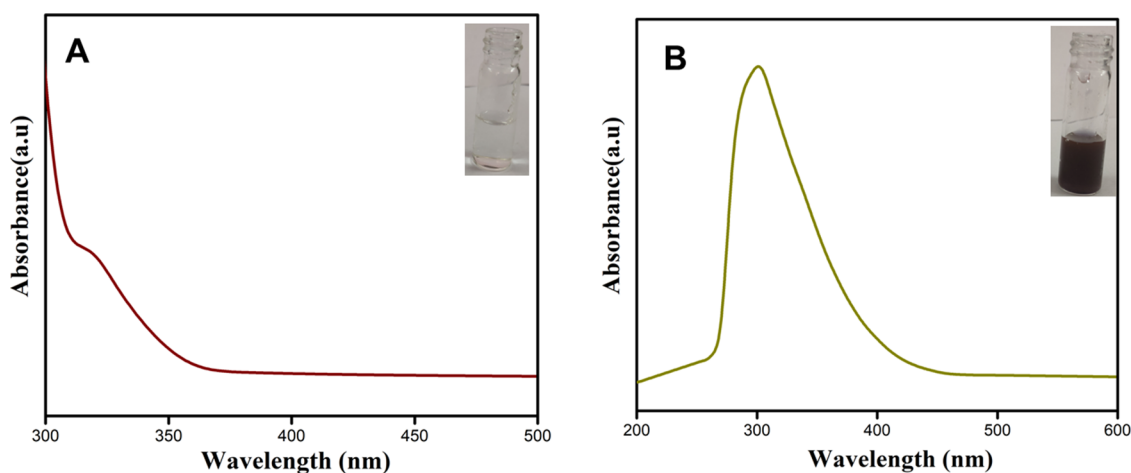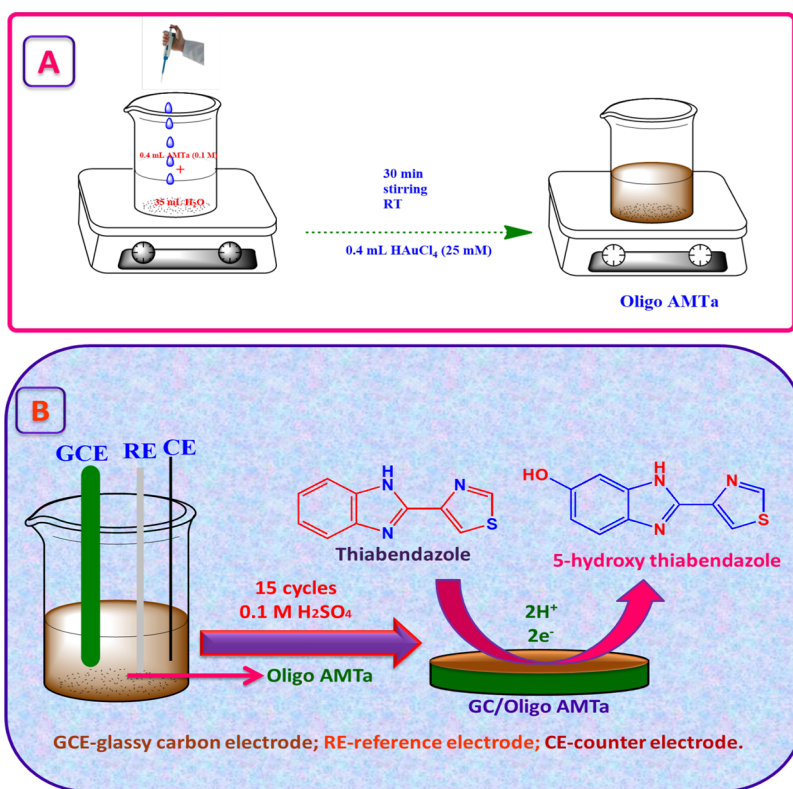

Figure 1. UV−visible spectra of (A) AMTa and (B) oligo AMTa in the NMP solvent.

reaction mixture was mixed with 500 μL of 25 mM HAuCl₄. After an hour of stirring the reaction mixture, a brownish-black solution appeared, signifying the synthesis of oligo AMTa (Scheme 1A). After centrifuging the mixture at 4300 rpm, 5 mL of the NMP solvent was used to dissolve the oligo AMTa powder, which had a brownish-black appearance. After several months at room temperature, the solution remained quite stable.

2.3. Fabrication of the Oligo AMTa-Modified GC Electrode. Here, 0.1 M H₂SO₄ was used as a supporting electrolyte for the formation of an oligomer on the GC electrode by the potentiodynamic method. The oligomer was formed on the GC electrode by 15 potential sweeps between −0.2 V and +1.7 V at a scan rate of 50 mV/s in oligo AMTa containing 0.1 M H₂SO₄. The modified electrode was termed the GC/oligo

AMTa electrode. Scheme 1B illustrates the attachment of the oligomer on the GC electrode.

3. RESULTS AND DISCUSSION

3.1. Characterization of Oligo AMTa by UV−Vis, FT-IR, XRD, XPS, TEM, and HR-MS. The $\pi-\pi^*$ transition of the heterocyclic triazole ring induced the absorption band of the AMTa monomer in the NMP solvent to be noticed at 317 nm (Figure 1A). The resulting oligo AMTa's UV−visible spectrum in NMP solvent is displayed in Figure 1B. It shows a sharp absorption peak at 301 nm. The observed blue shift indicated the formation of the oligomer. Here, auric acid is an oxidizing agent. Oxidation of AMTa generates the electrons which reduce the auric ions into "Au⁺" ions. The reduced auric acid was

oxidized AMTa into oligo AMTa. There is no absorption band appearing at 510 nm, which indicates that there is no nanoparticle formation. This means that AMTa does not completely reduce the Au^{3+} into Au^0. It was further confirmed by the XPS spectrum and CV.

Also, FT-IR spectroscopy was applied to evaluate the obtained AMTa and oligo AMTa. The FT-IR spectra of the solid AMTa monomer and synthesized oligo AMTa are shown in Figure 2. Table S1 provides an overview of the IR bands for
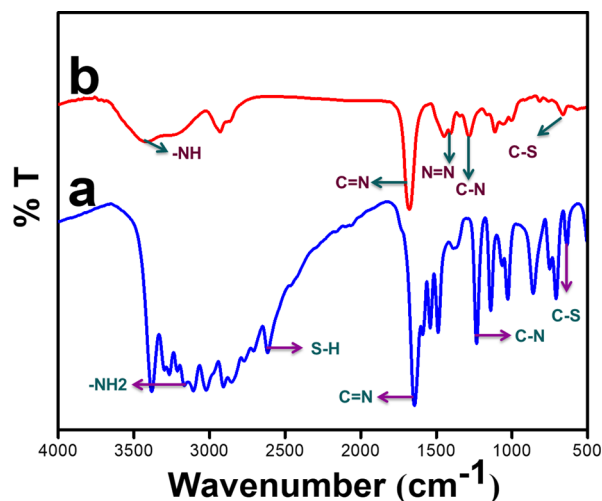

Figure 2. FT-IR spectra obtained for powder (a) AMTa and (b) oligo AMTa.

AMTa and oligo AMTa as well as their assignments. In contrast to AMTa, the oligo AMTa demonstrates a new peak at 1449 cm^{-1} (curve b). Curve a shows an insignificant stretching doublet for AMTa at 3298 and 3268 cm^{-1}.[37,38] Curve b shows that these bands do not occur for oligo AMTa, demonstrating that $-NH_2$ groups are involved in the oligomerization process.[37,38] Therefore, oligo AMTa exhibits a stretching band at 1449 cm^{-1} corresponding to $-N=N-$,[37,38] demonstrating that during oligomerization, $-NH_2$ groups were converted into $-N=N-$ groups; in contrast, AMTa did not exhibit this peak. The curve further shows that the AMTa has a peak at 2615 cm^{-1}, correlating to the $-SH$ group. This peak disappeared at oligo AMTa, indicating that the $S-S$[37,38] linkage is the mechanism by which oligomerization occurs (curve b). Beyond the peak displayed by the AMTa with greater shift, the oligo AMTa exhibits a peak at 1678 cm^{-1} (curve b).[37,38] The peaks at 1678 and 1680 cm^{-1} demonstrate the $C=N$ stretching vibration. The $C-N$ stretching vibration is apparent by the peak that oligo AMTa presents at 1282 cm^{-1}.[37,38,53]

The XRD patterns of the solid AMTa monomer and synthesized oligo AMTa are shown in Figure S1. Powdered AMTa (curve a) typically exhibits diffraction peaks corresponding to a crystal system identified as orthorhombic, with lattice parameters $a = 8.0$ Å, $b = 9.2$ Å, and $c = 10.5$ Å. The XRD pattern suggests an average crystal size of approximately 30 nm. In contrast, the XRD analysis of powdered oligo AMTa (curve b) at low angles reveals several key details about its crystal structure. The lattice parameters measured from the XRD peaks correspond to a crystal system identified as monoclinic, with specific lattice constants of $a = 7.2$ Å, $b = 10.5$ Å, $c = 8.8$ Å, and $\beta = 95°$ (curve b). The XRD pattern indicates an average crystal size of approximately 20 nm, suggesting a nanocrystalline nature.

The space group determined from the XRD data indicates a symmetry that includes a 2-fold rotation axis and a mirror plane perpendicular to it. The space group for AMTa indicates orthorhombic symmetry, while oligo AMTa belongs to the space group reflecting its monoclinic symmetry. The XRD pattern of powdered AMTa (curve a) typically exhibits distinct peaks corresponding to its crystalline structure. XRD peaks include the (100) plane at approximately 10.5°, the (110) plane at around 19.9°, and the (200) plane at approximately 23.6°. These peaks correspond to specific crystallographic planes within the AMTa structure, providing information about the spacing between the atomic layers and the orientation of atoms within the crystal lattice. For oligo AMTa powder (curve b), the exact XRD planes and corresponding 2θ values are as follows: (110) at 13.5°, (211) at 23.9°, and (310) at 44.4°. These specific peaks correspond to the crystallographic planes in the monoclinic crystal structure of oligo AMTa. These XRD findings reveal distinct crystalline structures and dimensions for AMTa and oligo AMTa, influencing their physical and chemical properties in various applications.

The oligo AMTa XPS spectra are displayed in Figure 3. Two-component peaks at 285.3 and 287.3 eV, which were linked to $C-N$ and $C=N$, respectively,[37,38,53] were identified using deconvolution of the oligo AMTa C 1s spectra (Figure 3A). The secondary amine nitrogen ($-NH-$) and imine nitrogen ($=NH$) are responsible for the two-component peaks at 399.9 and 396.7 eV in the oligo AMTa N 1s spectra, respectively[37,38,53] (Figure 3B). At 285.3 eV, $C-N$ was demonstrated to have the predominant binding energy (BE). The $C=N$ is represented by the tiny peak at 287.3 eV. The chemical oligomerization in this scenario proceeds via $-NH$ and $N=N$, as evidenced by the lack of BE at 284.0 eV for $C-C$ or $C=C$.[37,38,53] At 163.8 and 167.9 eV, the S 2p region of the oligo AMTa deconvoluted into two component peaks, which were linked to sulfur bound to sulfur and heterocyclic sulfur, respectively[37,38,53] (Figure 3C). However, 84.8 eV in the case of oligo AMTa suggests that the gold atom does not exist as Au^0 (Figure 3D). It verifies that no gold nanoparticle has been developed.

HR-TEM was utilized to analyze the morphology of oligo AMTa. The HR-TEM images of oligo AMTa at several magnifications are displayed in Figure 4. The HR-TEM images exhibit the cloud-like structure of oligo AMTa (Figure 4a–c). Here, a greater number of spherical particles congregate together and form a cloudlike structure. The oligomeric network was also seen in the background of the TEM image. The crystallinity nature of oligo AMTa is demonstrated by its SAED pattern (Inset: Figure 4a).

Furthermore, HR-MS was employed to investigate the resulting oligo AMTa. The HR-MS of oligo AMTa is displayed in Figure 5. The measured m/z peaks range from 285 to 1420, which are indicative of distinct molecular ion species. The molecular mass of the AMTa monomer ($m/z = 116$) was absent in the HR-MS spectrum, suggesting that AMTa may have been converted to an oligomer or polymer. Figure 5 shows the HR-MS results of oligo AMTa. The peak at $m/z = 564.08$ corresponds to the molecular ion of five monomers attached to a chain, indicating the formation of oligomeric AMTa. In addition, the presence of a tetrameric form of AMTa was confirmed from the m/z peak at 435.03. The presence of m/z peaks at 685.43 and 784.49 correspond to molecular ions of four and five monomers attached with metallic gold.

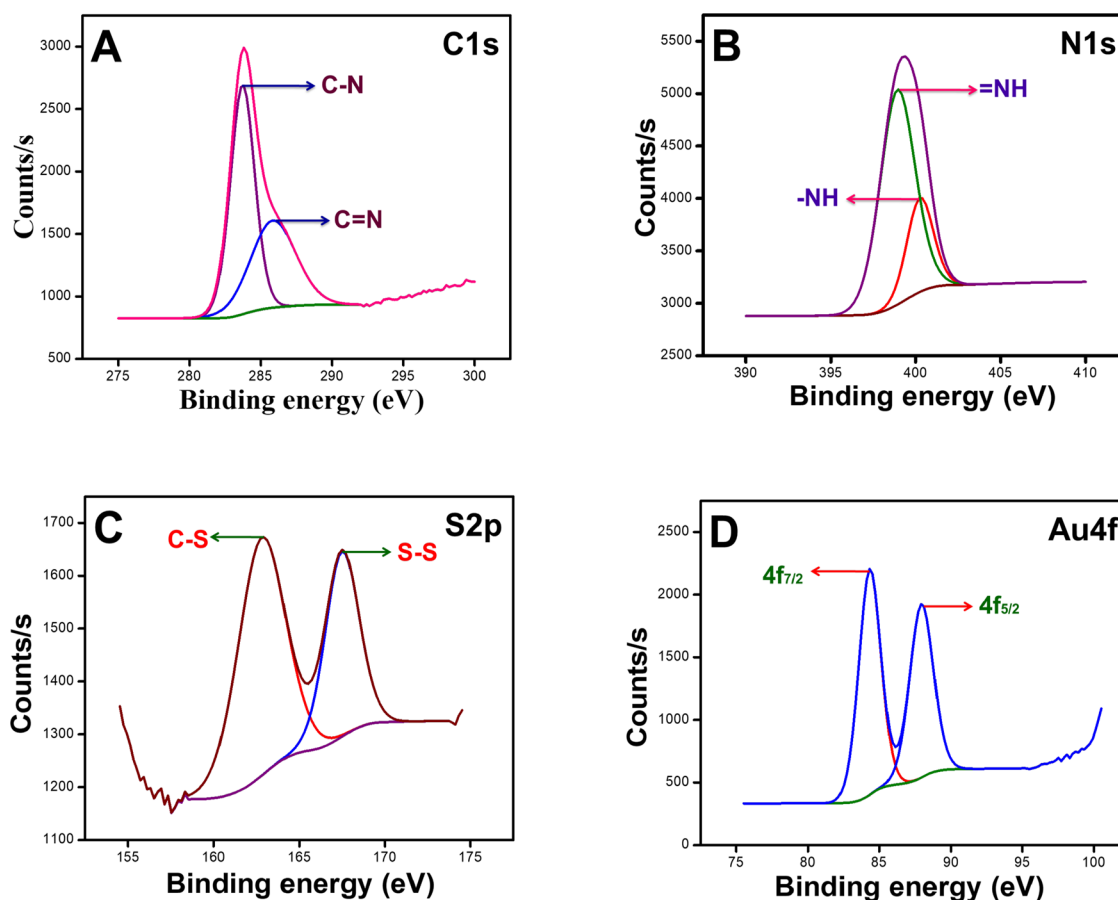**3.2. Potentiodynamic Particles Formation of Oligo AMTa on the GC Electrode.** Electrochemical polymerization

Figure 3. XPS spectra of powder oligo AMTa: (A) C 1s, (B) N 1s, (C) S 2p, and (D) Au 4f regions.
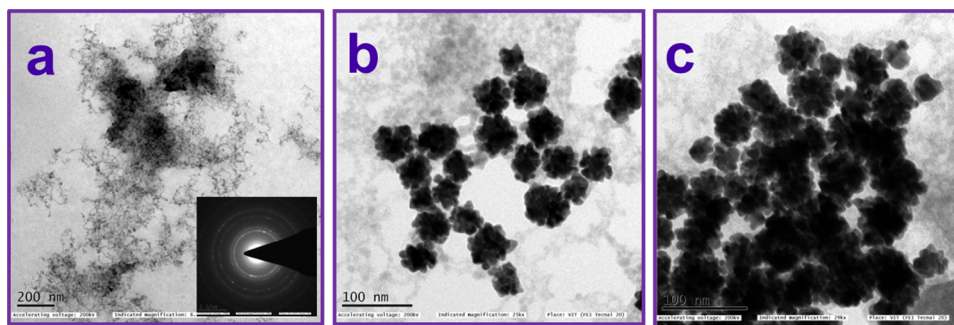

Figure 4. TEM images of oligo AMTa recorded at different magnifications (a–c). Inset of a: SAED pattern of oligo AMTa.

of AMTa has already been reported.[38] In this study, we attempt to modify chemically polymerized AMTa on the GC surface using a potentiodynamic method and check their electrocatalytic activities. Figure 6 shows the potentiodynamic formation of oligo AMTa (15 cycles) on a GC electrode containing 0.1 M H_2SO_4. While comparing this oligo AMTa (Figure 6) with the reported electropolymerized poly AMTa film, there are no oxidation and oxidation peaks observed in this case. This does not mean failure in the attachment of the oligo AMTa. CVs obtained for oligo AMTa on a GC electrode deposited by 15 cycles in 0.1 M H_2SO_4 at scan rates of 1000–10,000 mV/s are shown in Figure S2. Both oxidation and oxidation peak currents were increased when the scan rate was increased. The plot of the cathodic peak current vs scan rate was linear with a correlation coefficient of 0.9988 (Figure S2: inset), suggesting that the redox reaction was a surface-confined

process. This redox peak of amine suggested the successful dots formation of oligo AMTa on the GC electrode. Furthermore, the successful formation of oligo AMTa particles on the GC surface was confirmed by SEM, EDAX, and EIS studies.

3.3. Characterization of Oligo AMTa Modified GC Substrates by SEM and EDAX. The oligo AMTa-modified GC plate was further characterized by SEM and EDAX. Figure 7 shows the SEM images and EDAX spectra of oligo AMTa coated on GC plates. Before cycling, the synthesized oligomer solution was coated on a GC substrate by drop casting. The SEM images of oligo AMTa coated GC plate exhibit spherical particles covered on the whole area can be clearly seen in the SEM image (Figure 7a). The particle size was found to be 2.6 μm. Then, the oligomer was coated on the GC substrate by a potentiodynamic method. The SEM image illustrates the formation of particle-like structures with uniform sizes of the oligomer after cycling in 0.1
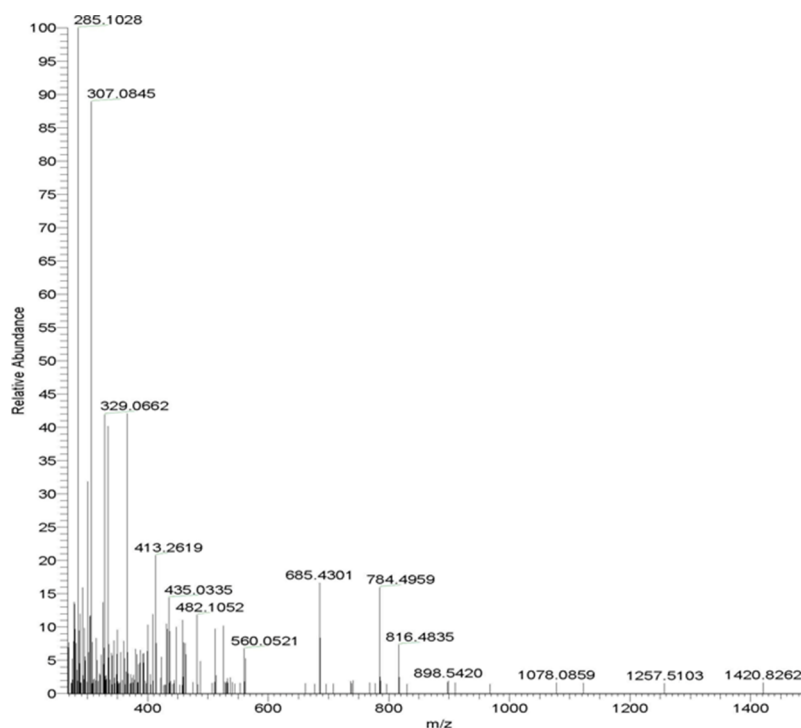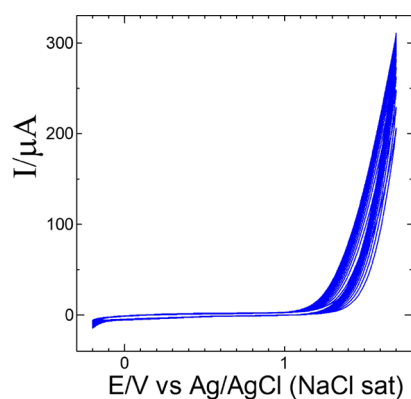
Figure 5. HR-MS of oligo AMTa.

Figure 6. Potentiodynamic formation of oligo AMTa (15 cycles) on a GC electrode in oligo AMTa containing 0.1 M H_2SO_4 at a scan rate of 50 mV/s.

M H_2SO_4 (Figure 7b). After electrocycling the size of the oligomer was reduced from 2.6 μm to 30 nm. The combined effects of acid-induced hydrolysis and electrochemical fragmentation can be responsible for the size reduction of oligo AMTa from 2.6 μm to 30 nm during electrocycling in 0.1 M H_2SO_4. The 0.1 M H_2SO_4 acidic environment facilitates the oligomer's hydrolysis, which breaks longer molecular chains into smaller fragments. In addition, the oligomer is further broken apart by oxidation and reduction processes brought on by applied electrical cycling. The oligomer is encouraged to reorganize into uniformly smaller nanoparticles by this combined mechanism of chemical and electrochemical breakdown, which results in a significant size reduction noticed in the SEM images. Further, the presence of nitrogen and sulfur elements in the oligomers before (Figure 7c) and after cycling (Figure 7d) was confirmed by the EDAX spectra. The peaks were observed at 0.2, 0.4, and 0.6 due to carbon, nitrogen and sulfur, respectively.

3.4. Electrochemical Characterization of Oligo AMTa-Modified GC Electrode.
Furthermore, electrochemical impedance spectroscopy (EIS) was used to characterize the resulting GC/oligo AMTa electrode. The Nyquist plots for unmodified GC and GC/oligo AMTa electrodes in 0.2 M PBS containing 1 mM $K_3/K_4[Fe(CN)_6]$ are shown in Figure 8. The R_{CT} values of 18 and 3 kΩ were found for unmodified GC and GC/oligo AMTa electrodes, respectively. Using the previously reported equation,[54−58] the k_{et} value for unmodified GC was 2.09 and 12.5×10^{-4} cm^2 for GC/oligo AMTa electrode. The acquired k_{et} values demonstrated that the electron transfer reaction of the oligo AMTa-modified electrode was easier than that of the unmodified electrode. The enhanced conductivity and electron transfer characteristics of the oligo AMTa coating are primarily responsible for the decreased R_{CT} value exhibited for the GC electrode modified by oligo AMTa when compared to those of the unmodified GC electrode. By introducing functional groups, the surface conductivity of the electrode is enhanced, and a greater efficiency of electron transfer between the electrode and the electrolyte is permitted. Further promoting faster and more efficient charge transfer processes is the improved surface's homogeneous particle-like structure, which enhances the active surface area. As a result, the EIS R_{CT} value is significantly lower.

The electroactive surface area (EAS) for the unmodified GC and GC/oligo AMTa electrodes was determined using the Anson equation.[54−58] The EAS values for the unmodified GC GC/oligo AMTa electrodes, respectively, were 0.06 and 0.38 cm^2. This substantial difference in EAS is attributed to the unique morphology of oligo AMTa resulting from its electroless deposition process. The oligo AMTa-modified electrode exhibited a surface area 6.3 times larger than that of the unmodified GC electrode, which can be primarily attributed to the formation of uniform-sized particles after cycling. This structural transformation likely enhanced the electrode's surface roughness and porosity, thereby increasing the active sites
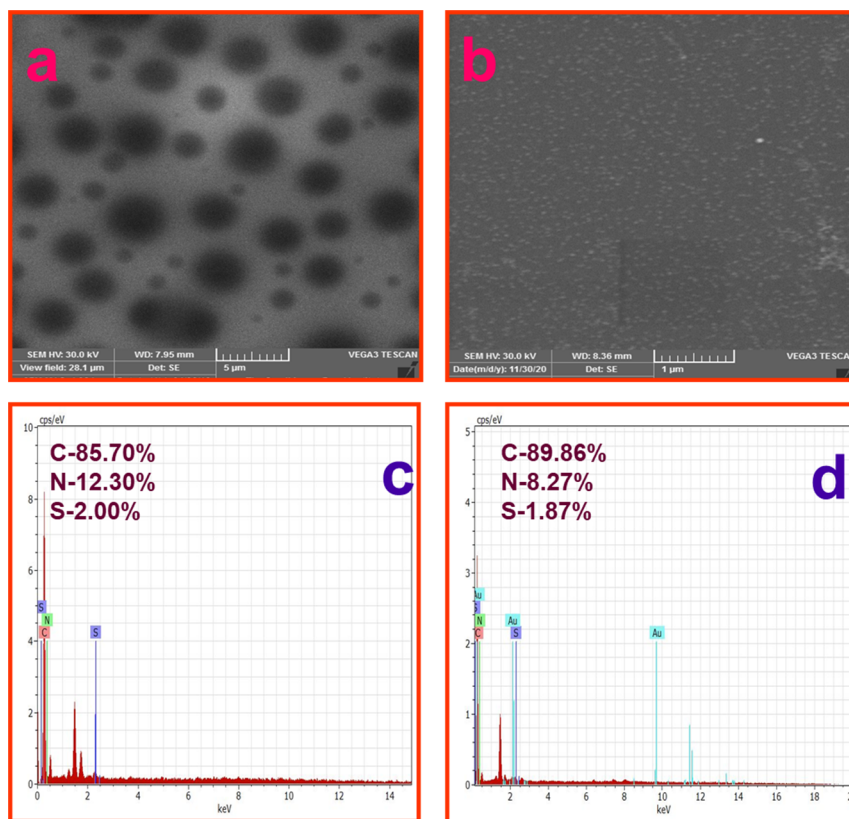
Figure 7. SEM and EDAX images of oligo AMTa before cycling (a, c) and oligo AMTa after cycling (b, d) coated on the GC substrate.
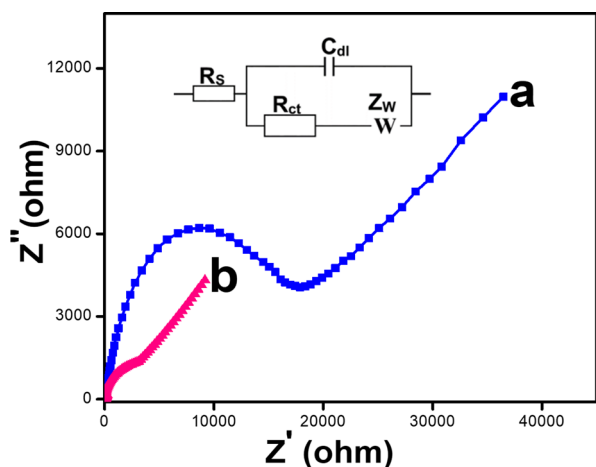

Figure 8. Nyquist plot for (a) unmodified GC and (b) GC/oligo AMTa electrodes in 1 mM $K_3[Fe(CN)_6]/K_4[Fe(CN)_6]$ containing 0.2 M PB solution (pH 7.2) at scanning frequencies from 0.01 to 100,000 Hz.

available for electrochemical reactions. The significant surface area improvement of the GC/oligo AMTa electrode underscores its potential for heightened sensitivity and efficiency in electrochemical sensing applications compared to the unmodified GC electrode.

The oligo AMTa-modified electrode possesses the highest electroactive surface area and electrical conductivity due to several key factors. First, the presence of amino ($-NH_2$) and thiol ($-SH$) functional groups in AMTa enhances the surface coverage and density of electroactive sites, increasing the electroactive surface area. Additionally, the conjugated structure of AMTa facilitates efficient electron transfer, resulting in

enhanced electrical conductivity compared to unmodified electrodes. These combined effects make the AMTa-modified electrode ideal for electrochemical applications, offering improved sensitivity and performance. Furthermore, the prepared oligo AMTa was characterized by CV. Figure S3 shows the CV obtained for the GC/oligo AMTa electrode in 0.2 M PB solution (pH 7.2) at a scan rate of 50 mV/s. From the CV, no gold oxide oxidation peak was observed in this potential window (0−1.4 V). It is clearly indicated that there is no formation of gold nanoparticles. Therefore, the AMTa does not completely reduce Au^{3+} to Au^0. This is already confirmed by the UV−visible and XPS techniques.

3.5. Electrochemical Oxidation of Thiabendazole (TBZ) at the OligoAMTa-Modified GC Electrode. Furthermore, the prepared oligo AMTa-modified GC electrode was used to electrochemically determine thiabendazole (TBZ). Utilizing unmodified GC and GC/oligo AMTa electrodes in 0.2 M PBS (pH 7.2) (Figure 9), 0.5 mM TBZ was oxidized. For the unmodified GC electrode, the oxidation peak was found at 1.13 V in the scrutinized potential range (curve a). In contrast, the GC/oligo AMTa electrode demonstrates a substantial oxidation in the peak at 0.89 V, when 0.5 mM TBZ is present (curve b). A 24 mV oxidation potential shift was observed between unmodified GC and GC/oligo AMTa electrodes, which indicates that the oxidation reaction is more facile in the GC/oligo AMTa electrode. The enhanced surface characteristics and additional functional groups of the oligo AMTa layer have been accountable for the 24 mV shift in oxidation potential between TBZ on the oligo AMTa modified GC electrode and the unmodified one. These modifications facilitate thiabendazole oxidation by improving electron transfer, lowering charge transfer resistance, and supplying particular binding sites. This
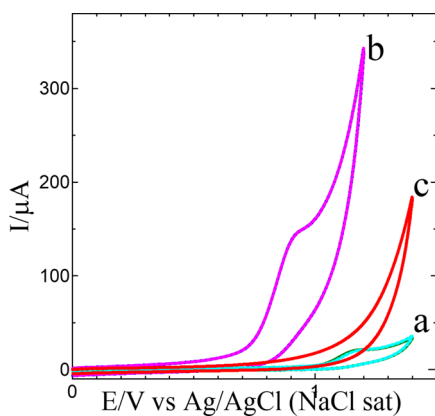
Figure 9. CVs obtained at (a) unmodified GC and (b) GC/oligo AMTa electrodes (solid line: first cycle and dotted line: after the eighth cycle) in the presence of 0.5 mM TBZ containing 0.2 M PB solution (pH 7.2) at a scan rate of 50 mV/s. (c) CV obtained for GC/oligo AMTa in the absence of TBZ.

change highlights the enhanced electrochemical performance brought about by surface modification.

The unmodified GC and GC/oligo AMTa electrodes exhibit oxidation currents for TBZ at 37 and 151 μA, respectively. The oxidation current for the TBZ in the oligo AMTa modified electrode was four-fold greater than that of unmodified GC electrodes, respectively. The highest electrochemical oxidation current for TBZ at the oligo AMTa-modified electrode is attributed to the enhanced surface properties provided by the oligo AMTa modification. The presence of amino and thiol groups in oligo AMTa significantly increases the adsorption affinity of TBZ molecules on the electrode surface through strong interactions such as hydrogen bonding, $\pi-\pi$ stacking, and coordination bonds. These interactions facilitate a more effective electron transfer process by bringing TBZ molecules closer to the electrode surface and stabilizing the intermediate species formed during oxidation. Additionally, the increased surface area and catalytic properties of the oligo AMTa-modified electrode contribute to an amplified electrochemical signal, resulting in a higher oxidation current for TBZ.

Two electron transfer processes utilizing 5-hydroxythiabendazole were proposed as a potential mechanism for the electrochemical oxidation of TBZ in neutral media (Scheme 1B). The electrochemical oxidation of TBZ on an oligo AMTa-modified electrode involves the initial adsorption of TBZ onto the modified electrode surface, facilitated by interactions such as hydrogen bonding and $\pi-\pi$ interactions with the amino and thiol groups of oligo AMT. Upon applying an appropriate potential, TBZ undergoes an initial electron transfer, forming a radical cation (TBZ·+). This radical cation can be further oxidized, resulting in the formation of a dication (TBZ^{2+}). The oligo AMT groups on the electrode stabilize these intermediates, possibly through coordination and hydrogen bonding. The final step involves the interaction of the dication with water, leading to the formation of various oxidation products and the release of protons. This modified electrode enhances the electrochemical response, providing a sharp and pronounced signal useful for the quantification of TBZ.

TBZ oxidation was accomplished by a diffusion-controlled method. This is supported by the accomplished linear plot of the current vs square root of the TBZ concentration (Figure S4). Furthermore, a more substantial increase in the current of TBZ was reported at pH 7 when the pH was adjusted from 3 to 11.

Consequently, TBZ was determined at a pH of 7.2, which is quite near 7.0 (Figure S5).

3.6. Sensitive and Selective Determination of TBZ by Differential Pulse Voltammetry (DPV) and Amperometry Techniques. TBZ was detected by DPV in a sensitive and selective manner. In 0.2 M PBS pH 7.2, Figure 10 displays the
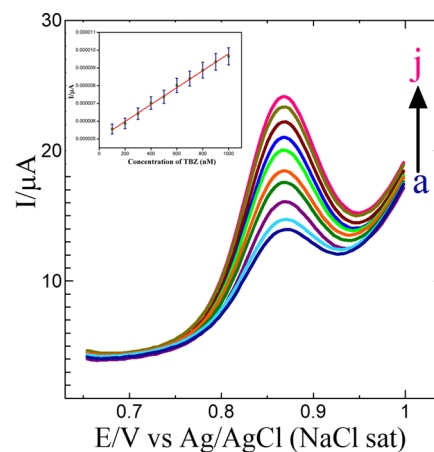

Figure 10. DPVs obtained for each increment (curves a−j) of 100 nM TBZ at the GC/oligo AMTa electrode in 0.2 M PB solution (pH 7.2). Inset: Plot of current vs concentration of TBZ.

DPVs of the stepwise addition of TBZ to the GC/oligo AMTa electrode. When 100 nM TBZ was administered, a TBZ peak was seen at 0.75 V (curve a). Progressively, the concentration of TBZ increased from 200 to 1000 nM (curves b−j), and the oxidation current increased further while the oxidation potential remained constant (a linear plot of TBZ reduction current versus concentration was obtained with $R^2 = 0.9987$) (Figure 10: inset).

TBZ measurement at a GC/oligo AMTa electrode employing an amperometric $i−t$ curve in a neutral medium (Figure 11). From 1 to 10 nM at the GC/oligo AMTa electrode, the current response and TBZ concentration had a linear relationship with a correlation coefficient of 0.9976 (Figure 11: inset). The $i−t$ curve demonstrated a steady current rise with every addition of 10 nM TBZ. Furthermore, the GC/oligo AMTa electrode was
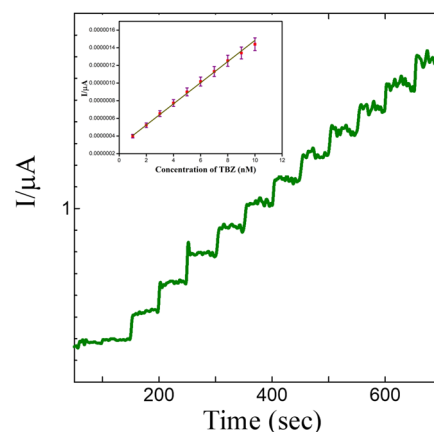

Figure 11. Amperometric $i−t$ curve for the determination of TBZ at GC/oligo AMTa electrode in 0.2 M PB solution (pH 7.2). Each addition increases the concentration of 1 nM TBZ at a regular interval of 50 s. $E_{app} = +1$ V.

employed to introduce TBZ in concentrations ranging from 1 nM to 0.5 mM for wide-range detection (Figure S6). The TBZ oxidation increases steadily as concentration increases (R^2 = 0.9996; Figure S6: inset), with a LOD of 1.8×10^{-11} M (S/N = 3). The current modified electrode's performance was compared to that of previously published nanomaterials and composite-modified electrodes (Table S2). The sensitivity of the GC/oligo AMTa electrode proved to be greater than that of sensors based on other materials.[48−52] The oligo AMTa modified electrode offers several distinct advantages over other reported modified electrodes for TBZ determination. Its modification enhances the surface conductivity and electron transfer rates, leading to higher sensitivity and lower detection limits. The uniform particle-like structure of the oligo AMTa layer increases the active surface area, facilitating greater interaction with TBZ molecules. This modification also introduces specific functional groups that improve selectivity by providing distinct binding sites for TBZ, reducing interference from other substances. Additionally, the simple and reproducible fabrication process of the oligo AMTa-modified electrode makes it practical for routine analysis. These combined benefits make the oligo AMTa-modified electrode a superior and efficient option for reliable TBZ detection.

Additionally, using the GC/oligo AMTa electrode, the selective detection of 10 nM TBZ containing the various interferences of biomolecules, cations, and anions was investigated (Figure S7). When 500 μM glucose and urea are administered, the electrochemical response of TBZ remains unaltered. The electrochemical activity of TBZ was unaltered when 500 μM K$^+$, Mg^{2+}, Ca^{2+}, Cl$^-$, F$^-$, CO$_3^{2-}$, and SO$_4^{2-}$ ions were introduced into the same solution. These findings suggest that the GC/oligo AMTa electrode is suitable for monitoring TBZ in a sensitive and selective manner.

3.7. Stability and Practical Application. TBZ in food, environmental, and agricultural goods can be determined electrochemically for several vital reasons. First, it protects food safety by monitoring and regulating the amounts of TBZ residues in food and agricultural goods. TBZ is frequently used as a fungicide in agriculture to prevent fungal diseases in crops. Consumers may be at risk for health problems if their diet has high TBZ residues.[46−52] Consequently, regulatory organizations can better enforce safety regulations and standards, safeguarding the public's health, by routinely checking the amounts of TBZ in food products. Furthermore, the environmental monitoring of TBZ residues in soil and water samples aids in the evaluation of the environmental impact of agricultural operations. If unchecked, TBZ may persist in the environment and contaminate water and soil.[46−52] Authorities can take action to reduce environmental pollution and protect ecosystems by maintaining monitoring of the levels of TBZ in environmental samples. In general, electrochemical determination offers a sensitive and reliable technique to measure TBZ residues in different samples, making it easier to comply with regulations and ensure the safety of food and the environment.[46−52]

Therefore, it is crucial that TBZ can be determined electrochemically in a variety of real samples. The GC/oligo AMTa electrode's practical applicability was proved by measuring TBZ in different samples such as tap water, pear juice, and water spinach (Figure S8). Before the experiment was started, tap water was diluted 14 times with 0.2 M PBS (pH 7.2). The GC/oligo AMTa electrode showed no electrochemical signal for tap water (Figure S8A: curve a). However, adding 100 nM TBZ to the real sample solution, on the other hand, results in a peak potential at 0.74 V (Figure S8A: curve b). Similarly, in

their current work, the determination of TBZ in pear juice (Figure S8B) and water spinach (Figure S8C) was also explored. Table S3 demonstrates that raising the amount of TBZ in tap water, pear juice, and water spinach improved the oxidation current, leading to a successful recovery.

Moreover, the GC/oligo AMTa electrode's durability was evaluated by measuring the DPV of 100 nM TBZ at 30 min intervals. The TBZ peak at 0.75 V is identical after eight consecutive measurements, with a relative standard deviation (RSD) of 1.3% (0.07%), demonstrating that the fabricated electrode is stable. All of these results confirm the GC/oligo AMTa electrode's long-term storage stability. Furthermore, the oxidation was measured by using five different GC/oligo AMTa electrodes. The modified electrode has an RSD of 1.4% (0.05%), indicating its exceptionally long-lasting and repeatable performance. The electrochemical oxidation of TBZ on the surface of an oligo AMTa-modified electrode is more stable due to several factors. First, the presence of amino and thiol groups on the oligo AMTa surface allows for strong adsorption and stabilization of TBZ molecules, reducing their propensity for desorption during electrochemical processes. Additionally, the modification enhances the surface passivation effect, preventing unwanted side reactions and minimizing electrode fouling, leading to improved stability of the oxidation process over repeated cycles.[59,60]

4. CONCLUSIONS

This study demonstrated an effortless method to produce novel oligomeric materials at ambient temperature. The oligo AMTa was generated chemically, and FT-IR, XRD, HR-MS, XPS, HR-TEM, and UV−visible spectroscopy were used to analyze it. The prepared oligomer has more spherical particles that congeal together to form a structure resembling a cloud, as shown by the HR-TEM pictures. The IR spectrum of oligo AMTa highlights the transformation of −NH$_2$ groups to −N═N− groups at 1449 cm^{-1} during oligomerization, distinguishing it from AMTa. Additionally, the absence of the −SH group peak at 2615 cm^{-1} suggests the involvement of S−S linkages in the oligomerization process. The XPS spectrum of oligo AMTa reveals a C═N peak at 287.3 eV, indicating oligomerization via −NH and N═N, as evidenced by the absence of peaks at 284.0 eV for the C−C or C═C bonds. The 84.8 eV peak in the XPS spectrum suggests no formation of Au^0, indicating the absence of gold nanoparticle formation. Powdered AMTa exhibits an orthorhombic crystal structure with an average crystal size of approximately 30 nm, as determined by XRD analysis. In contrast, powdered oligo AMTa displays a monoclinic crystal system, indicating a nanocrystalline nature with an average crystal size of approximately 20 nm. The XRD patterns revealed distinct peaks corresponding to their respective crystal structures, providing insights into the symmetry and atomic arrangements of AMTa and oligo AMTa. Furthermore, the HR-MS spectrum confirmed oligo AMTa's structure, showing peaks at m/z 564.08 and 435.03, indicative of five monomers in a chain and a tetrameric form of AMTa, respectively. Additionally, the oligomer was potentio-dynamically linked to the GC surface before being further characterized by SEM, EDAX, CV, and EIS investigations. During electrocycling in 0.1 M H$_2$SO$_4$, oligo AMTa underwent a substantial size reduction from 2.6 μm to 30 nm. This reduction is attributed to acid-induced hydrolysis, where the acidic environment facilitated the breakdown of longer molecular chains into smaller fragments. Additionally, electrochemical processes induced oxidation and reduction reactions that further

fragmented the oligomer, promoting its reorganization into uniformly smaller nanoparticles, as observed in SEM images. The oligo AMTa-modified electrode boasts the highest electroactive surface area due to the abundant amino ($-NH_2$) and thiol ($-SH$) functional groups, enhancing surface coverage. Additionally, its conjugated structure facilitates efficient electron transfer, elevating electrical conductivity compared with unmodified electrodes. Compared to the unmodified GC electrode, the oligomer-modified electrode demonstrated superior electrocatalytic activity toward the oxidation of TBZ. The overall electrochemical oxidation mechanism of TBZ at oligo AMT-modified electrode involves adsorption, electron transfer steps, intermediate stabilization, and the formation of final oxidation products. The modification of the electrode surface with oligo AMT enhances these processes, leading to better analytical performance in detecting TBZ. After that, the film was used to measure the sensitivity of TBZ and it was discovered that the LOD was 1.8×10^{-11} M (S/N = 3). The current modified electrode was effectively applied in the field to measure TBZ in samples of tap water, water spinach, and pear juice. Because of the better adsorption of TBZ made possible by amino and thiol groups on the oligo AMTa surface, which reduces desorption during oxidation, the electrochemical oxidation of TBZ on an oligo AMTa-modified electrode is more stable. Furthermore, by facilitating the development of stable intermediate species, the modified electrode may increase the stability of the oxidation process.

ASSOCIATED CONTENT

Supporting Information

The Supporting Information is available free of charge at https://pubs.acs.org/doi/10.1021/acsomega.4c04959.

> XRD pattern of powder AMTa and oligo AMTa; FT-IR spectrum of GCN powder; CVs obtained for oligo AMTa on the GC electrode deposited by 15 cycles in 0.1 M H_2SO_4 at different scan rates 1000−10000 mV/s; CV obtained for the GC/oligo AMTa electrode in 0.2 M PB solution (pH 7.2) at a scan rate of 50 mV/s; CVs obtained for 0.5 mM TBZ at GC/oligo AMTa electrode in 0.2 M PB solution (pH 7.2) at different scan rates 10−100 mV/s; CVs obtained for the GC/oligo AMTa electrode in the presence of 0.5 mM TBZ in different pH solutions 3, 5, 7, 9, and 11 at a scan rate of 50 mV/s; amperometric $i-t$ curve for the determination of TBZ at the GC/oligo AMTa electrode in 0.2 M PB solution (pH 7.2); each addition increases the concentration from 0.000001 to 0.5 mM TBZ at GC/oligo AMTa electrode in 0.2 M PB solution (pH 7.2) at a regular interval of 50 s; amperometric $i-t$ curve for (a) 10 nM TBZ and in the presence of 500 μM each Na^+, K^+, Mg^{2+}, Ca^{2+}, Cl^-, F^-, CO_3^{2-}, SO_4^{2-}, glucose and urea; E_{app} = +1 V; DPVs obtained for tap water and after the addition of (100−900 nM TBZ) to tap water at GC/oligo AMTa electrode in 0.2 M PB solution (pH 7.2); DPVs obtained for pear juice and after the addition of (100−900 nM TBZ) to pear juice at GC/oligo AMTa electrode in 0.2 M PB solution (pH 7.2); DPVs obtained for water spinach and after the addition of (100−900 nM TBZ) to water spinach at the GC/oligo AMTa electrode in 0.2 M PB solution (pH 7.2); FT-IR peaks and their assignments are obtained for powder AMTa and oligo AMTa (Table S1); comparison of the electrochemical performance of GC/oligo AMTa electrode toward the detection of thiabendazole with the reported studies (Table S2); and obtained good recovery results indicate that the oligo AMTa-modified electrode could be applied for the determination of TBZ in tap water, pear juice, and water spinach samples (Table S3) (PDF)

AUTHOR INFORMATION

Corresponding Author

Sirikanjana Thongmee — *Department of Physics, Faculty of Science, Kasetsart University, Bangkok 10900, Thailand;* orcid.org/0000-0001-8294-9997; Email: fscisjn@ku.ac.th

Authors

Veeramani Mangala Gowri — *Department of Physics, Faculty of Science, Kasetsart University, Bangkok 10900, Thailand; Department of Chemistry, The Gandhigram Rural Institute, 624 302 Dindigul, Tamilnadu, India*

Pontagarn Chanpuang — *Department of Physics, Faculty of Science, Kasetsart University, Bangkok 10900, Thailand*

Warit Bunrueang — *Department of Physics, Faculty of Science, Kasetsart University, Bangkok 10900, Thailand*

Tanawat Imboon — *Department of Physics, Faculty of Science, Kasetsart University, Bangkok 10900, Thailand*

Dusadee Khamboonrueang — *Faculty of Science and Technology, Nakhon Sawan Rajabaht University, Mueang District, Nakhon Sawan 60000, Thailand*

Chaisak Issro — *Department of Physics, Faculty of Science, Burapha University, Chonburi 10131, Thailand*

Mutsuhiro Shima — *Department of Materials Science and Processing, Graduate School of Natural Science and Technology, Gifu University, Yanagida, Gifu 501-1193, Japan*

Complete contact information is available at: https://pubs.acs.org/10.1021/acsomega.4c04959

Notes

The authors declare no competing financial interest.

REFERENCES

(1) Namsheer, K.; Rout, C. S. Conducting Polymers: A Comprehensive Review on Recent Advances in Synthesis Properties and Applications. *RSC Adv.* **2021**, *11*, 5659.

(2) Ding, H.; Hussein, A. M.; Ahmad, I.; Latef, R.; Abbas, J. K.; Ali, A. T. A.; Saeed, S. M.; Abdulwahid, A. S.; Ramadan, M. F.; Rasool, H. A.; Elawady, A. Conducting Polymers in Industry: A Comprehensive Review on The Characterization, Synthesis and Application. *Alex. Eng. J.* **2024**, *88*, 253.

(3) Poddar, A. K.; Patel, S. S.; Patel, H. D. Synthesis, Characterization and Applications of Conductive Polymers: A Brief Review. *Polym. Adv. Technol.* **2021**, *32*, 4616.

(4) Kumar, D.; Sharma, R. C. Advances in Conductive Polymers. *Eur. Polym. J.* **1998**, *34*, 1053.

(5) Tajika, S.; Beitollahi, H.; Nejadc, F. G.; Shoaiec, I. S.; Khalilzadeh, M. A.; Asle, M. S.; Le, Q. V.; Zhangg, K.; Jang, H. W.; Shokouhimehr, M. Recent Developments in Conducting Polymers: Applications for Electrochemistry. *RSC Adv.* **2020**, *10*, 37834.

(6) Mattam, L. B.; Bijoy, A.; Thadathil, D. A.; George, L.; Varghese, A. Conducting Polymers: A Versatile Material for Biomedical Applications. *ChemistrySelect* **2022**, *7*, No. e202201765.

(7) Lin, S.; Wu, Q.; Lu, Y. Recent Progress of The Application of Electropolymerization in Batteries and Supercapacitors: Specific Design of Functions in Electrodes. *ChemElectroChem.* **2024**, *11*, No. e202300776.

(8) Maziza, A.; Ozgur, E.; Bergauda, C.; Uzun, L. Progress in Conducting Polymers for Biointerfacing and Biorecognition Applications. *Sens. Actuators Rep.* **2021**, *3*, No. 1000035.

(9) Lakard, B. Electrochemical Biosensors Based on Conducting Polymers: A Review. *Appl. Sci.* **2020**, *10*, 6614.

(10) Tran, V. V.; Lee, S.; Lee, D.; Le, H. Recent Developments and Implementations of Conductive Polymer-Based Flexible Devices in Sensing Applications. *Polymer* **2022**, *14*, 3730.

(11) Zhang, B.; Chen, J.; Liu, B.; Tang, D.; Dass, P. M. Amplified Electrochemical Sensing of Lead Ion Based on DNA-Mediated Self-Assembly-Catalyzed Polymerization. *Biosens. Bioelectron.* **2015**, *69*, 230.

(12) Tadesse, M. G.; Ahmmed, A. S.; Lubben, J. F. Review on Conductive Polymer Composites for Supercapacitor Applications. *J. Compos. Sci.* **2024**, *8*, 53.

(13) Chen, S.; Yu, Z.; Wang, Y.; Tang, J.; Zeng, Y.; Liu, X.; Tang, D. Block-Polymer-Restricted Sub-nanometer Pt Nanoclusters Nanozyme-Enhanced Immunoassay for Monitoring of Cardiac Troponin I. *Anal. Chem.* **2023**, *95*, 14494.

(14) Luong, J. H. T.; Narayan, T.; Solanki, S.; Malhotra, B. D. Recent Advances of Conducting Polymers and Their Composites for Electrochemical Biosensing Applications. *J. Funct. Biomater.* **2020**, *11*, 71.

(15) Singh, N.; Riaz, U. Recent Trends on Synthetic Approaches and Application Studies of Conducting Polymers and Copolymers: A Review. *Polym. Bull.* **2022**, *12*, 10377.

(16) Marjanovic, G. I. Recent Advances in Polyaniline Research: Polymerization Mechanisms, Structural Aspects, Properties and Applications. *Synth. Met.* **2013**, *177*, 1.

(17) Murad, A. R.; Iraqi, A.; Aziz, S. B.; Abdullah, S. N.; Brza, M. A. Conducting Polymers for Optoelectronic Devices and Organic Solar Cells: A Review. *Polymer* **2020**, *12*, 2627.

(18) Esfahani, N. N.; Dastan, D.; Alizadeh, A.; Shirvanisamani, P.; Rozati, M.; Ricciardi, E.; Lewis, B.; Aphale, A.; Toghraie, D. A Critical Review on Intrinsic Conducting Polymers and Their Applications. *J. Ind. Eng. Chem.* **2023**, *125*, 14.

(19) Zeng, R.; Luo, Z.; Zhang, L.; Tang, D. Platinum Nanozyme-Catalyzed Gas Generation for Pressure-Based Bioassay Using Polyaniline Nanowires-Functionalized Graphene Oxide Framework. *Anal. Chem.* **2018**, *90*, 12299.

(20) Shu, J.; Qiu, Z.; Tang, D. Self-Referenced Smartphone Imaging for Visual Screening of H_2S Using Cu_xO-Polypyrrole Conductive Aerogel Doped with Graphene Oxide Framework. *Anal. Chem.* **2018**, *90*, 9691.

(21) Shu, J.; Qiu, Z.; Lv, S.; Zhang, K.; Tang, D. Cu^{2+} Doped SnO_2 Nanograin/Polypyrrole Nanospheres with Synergic Enhanced Properties for Ultrasensitive Room-Temperature H_2S Gas Sensing. *Anal. Chem.* **2017**, *89*, 11135.

(22) Paramshetti, S.; Angolkar, M.; Garg, A.; Ravi, G.; Fatease, A. A.; Alshahrani, S. M.; Osmani, R. A. Revolutionizing Drug Delivery and Therapeutics: The Biomedical Applications of Conductive Polymers and Composites-Based Systems. *Pharmaceutics* **2023**, *15*, 1204.

(23) Le, C. V.; Yoon, H. Advances in the Use of Conducting Polymers for Healthcare Monitoring. *Int. J. Mol. Sci.* **2024**, *25*, 1654.

(24) Beygisangchin, M.; Rashid, S. A.; Shafie, S.; Sadrolhosseini, A. R.; Lim, H. N. Preparations, Properties, And Applications of Polyaniline and Polyaniline Thin Films—A Review. *Polymer* **2021**, *13*, 2003.

(25) Ji, W. F.; Chu, C. M.; Hsu, S. C.; Lu, Y. D.; Yu, Y. C.; Santiago, K. S.; Yeh, J. M. Synthesis and Characterization of Organo-Soluble Aniline Oligomer Based Electroactive Doped with Gold Nanoparticles, and Application to Electrochemical Sensing of Ascorbic Acid. *Polymer* **2017**, *128*, 218.

(26) Majeed, A. H.; Mohammed, L. A.; Hammoodi, O. G.; Sehgal, S.; Alheety, M. A.; Saxena, K. K.; Dadoosh, S. A.; Mohammed, K.; Jasim, M. M.; Salmaan, N. U. A Review on Polyaniline: Synthesis, Properties, Nanocomposites, and Electrochemical Applications. *Int. J. Polym. Sci.* **2022**, *2022*, No. 9047554.

(27) Sumdani, G.; Islam, M. R.; Yahaya, A. N. A.; Safie, S. Recent Advancements in Synthesis, Properties, and Applications of Conductive Polymers for Electrochemical Energy Storage Devices: A Review. *Polym. Eng. Sci.* **2021**, *62*, 269.

(28) Biyikogulu, M.; Ciftci, H. Chemical Synthesis and Characterization of Soluble Conducting Poly(2-Aminothiazole). *Polym. Bull.* **2013**, *70*, 2843.

(29) Tiwari, M.; Gupta, S.; Prakash, R. One Pot Synthesis of Coordination Polymer 2,5-Dimercapto-1,3,4-Thiadiazole—Gold and Its Application in Voltammetric Sensing of Resorcinol. *RSC Adv.* **2014**, *4*, 25675.

(30) Huang, S.; Ma, C.; Li, C.; Min, C.; Du, P.; Xia, Y.; Yang, C.; Huang, Q. Facile Synthesis, Characterization of Poly-2-Mercapto-1,3,4-Thiadiazole Nanoparticles for Rapid Removal of Mercury and Silver Ions from Aqueous Solutions. *Polymer* **2018**, *10*, 150.

(31) Savateev, A.; Pronkin, S.; Epping, J. D.; Willinger, M. G.; Antoniettia, M.; Dontsova, D. Synthesis of An Electronically Modified Carbon Nitride from a Processable Semiconductor, 3-Amino-1,2,4-Triazole Oligomer, via a Topotactic-Like Phase Transition. *J. Mater. Chem. A* **2017**, *5*, 8394.

(32) Yildirim, M.; Kaya, I. A Comparative Study of Aminothiazole-Based Polymers Synthesized by Chemical Oxidative Polymerization. *Synth. Met.* **2012**, *162*, 436.

(33) Solamaz, R.; Kardas, G. Electrochemical Synthesis and Characterization of Poly-2-Aminothiazole. *Prog. Org. Coat.* **2009**, *64*, 81.

(34) Lamanna, M. E.; Horra, E.; Jacobo, S.; Accorso, N. B. Synthesis of an Organic Semiconductor by Polymerization of 3-Amino-1,2,4-Triazole. *React. Funct. Polym.* **2009**, *69*, 759.

(35) Kalimuthu, P.; John, S. A. Electropolymerized Film of Functionalized Thiadiazole on Glassy Carbon Electrode for The Simultaneous Determination of Ascorbic Acid Dopamine and Uric Acid. *Bioelectrochemistry* **2009**, *77*, 13.

(36) Kalimuthu, P.; John, S. A. Simultaneous Determination of Ascorbic Acid, Dopamine, Uric Acid and Xanthine Using a Nano-structured Polymer Film Modified Electrode. *Talanta* **2010**, *80*, 1686.

(37) Kalimuthu, P.; John, S. A. Simultaneous Determination of Epinephrine, Uric Acid and Xanthine in The Presence of Ascorbic Acid Using an Ultrathin Polymer Film Of 5-Amino-1,3,4-Thiadiazole-2-Thiol Modified Electrode. *Anal. Chim. Acta* **2009**, *647*, 97.

(38) Revin, S. B.; John, S. A. Electropolymerization of 3-Amino-5-Mercapto-1,2,4-Triazole on Glassy Carbon Electrode and Its Electro-catalytic Activity Towards Uric Acid. *Electrochim. Acta* **2011**, *56*, 8934.

(39) Lin, L.; Peng, Z.; Yang, C. L.; Wang, M. Y.; Zha, Y. B.; Liu, L. L.; Zeng, S. D. Determination of imidacloprid, carbendazim and thiabendazole residues in vegetables and fruits by HPLC. *Adv. Mater. Res.* **2013**, *781*, 1392.

(40) Razman, A. Determination of Thiabendazole in Citrus Fruits by Ultraviolet Spectrophotometry. *Analyst* **1974**, *99*, 120.

(41) Reyes, J. F. G.; Martinez, E. J. L.; Barrales, P. O.; Diaz, A. M. Determination of Thiabendazole Residues in Citrus Fruits Using a Multicommuted Fluorescence-Based Optosensor. *Anal. Chim. Acta* **2006**, *557*, 95.

(42) Llorent-Martínez, E. J.; Fernández-de Córdova, M. L.; Ruiz-Medina, A.; Ortega-Barrales, P. Fluorimetric Determination of

Thiabendazole Residues in Mushrooms Using Sequential Injection Analysis. *Talanta* **2012**, *96*, 190.

(43) Yu, Q. W.; Sun, H.; Wang, K.; He, H. B.; Feng, Y. Q. Monitoring of Carbendazim and Thiabendazole in Fruits and Vegetables by Sio_2@Nio-Based Solid-Phase Extraction Coupled to High-Performance Liquid Chromatography-Fluorescence Detector, Food Anal. *Methods* **2017**, *10*, 2892.

(44) Choi, S. I.; Han, X.; Lee, S. J.; Men, X.; Oh, G.; Lee, D. S.; Lee, O. H. Validation of an Analytical Method for The Determination of Thiabendazole in Various Food Matrices. *Sep.* **2022**, *9*, 135.

(45) Khrushchev, A. Y.; Akmaev, E. R.; Belozerova, O. A.; Shmygarev, V. I.; Gulyaeva, A. Y. Determination of Trace Amounts of Thiabendazole in Fruit Juices Using Internal Standard-Based SERS Method. *Vib. Spectrosc.* **2023**, *127*, No. 103544.

(46) Budetic, M.; Kopf, D.; Dandic, A.; Samardzic, M. Review of Characteristics and Analytical Methods for Determination of Thiabendazole. *Mol.* **2023**, *28*, 3926.

(47) Noori, J. S.; Mortensen, J.; Geto, A. Recent Development on The Electrochemical Detection of Selected Pesticides: A Focused Review. *Sens.* **2020**, *20*, 2221.

(48) Yang, J. C.; Zhang, D. F.; Wang, L. L.; Long, N.; Zhang, M. H.; Zhang, L.; An, L. Electrochemical Method for High Sensitive Detection of Thiabendazole and Its Interaction with Human Serum Albumin. *Food Anal. Methods* **2015**, *8*, 507.

(49) Dong, Y.; Yang, L.; Zhang, L. Simultaneous Electrochemical Detection of Benzimidazole Fungicides Carbendazim and Thiabendazole Using a Novel Nano-Hybrid Material Modified Electrode. *J. Agric. Food Chem.* **2017**, *65*, 727.

(50) Li, J.; Ma, X.; Zhang, M.; Li, D.; Yuan, Y.; Fan, Y.; Xie, X.; Guo, L.; Zeng, G. Preparation of Molecularly Imprinted Polymer Sensor on Electrochemically Reduced Graphene Oxide Modified Electrode for Selective Probing of Thiabendazole. *J. Electrochem. Soc.* **2019**, *166*, B84.

(51) Cheng, F.; Liao, X.; Huang, Z.; Xu, L.; Zhou, Y.; Zhang, X. Highly Sensitive Detection of Thiabendazole Residues in Food Samples Based on Multiwall Carbon Nanotubes Decorated Two-Dimensional Layered Molybdenum Disulfide. *Food Anal. Methods* **2020**, *13*, 811.

(52) Ribeiro, F. W. P.; Oliveira, R. C.; Oliveira, A. G.; Nascimento, R. F.; Beckerb, H.; Neto, P. L.; Correia, A. N. Electrochemical Sensing of Thiabendazole in complex samples using boron-doped diamond electrode. *J. Electroanal. Chem.* **2020**, *866*, No. 114179.

(53) Kannan, P.; John, S. A. Fabrication of Conducting Polymer-Gold Nanoparticles Film on Electrodes Using Monolayer Protected Gold Nanoparticles and Its Electrocatalytic Application. *Electrochim. Acta* **2011**, *56*, 7029.

(54) Gowri, V. M.; Ajith, A.; John, S. A. Systematic Study on Morphological, Electrochemical Impedance, and Electrocatalytic Activity of Graphitic Carbon Nitride Modified on a Glassy Carbon Substrate from Sequential Exfoliation in Water. *Langmuir* **2021**, *37*, 10538.

(55) Gowri, V. M.; Ajith, A.; John, S. A. Different Modes of Attachment of Graphitic Carbon Nitrides on Glassy Carbon Electrode and Their Electrocatalytic Activity. *Microchem. J.* **2023**, *191*, No. 108818.

(56) García Rojas, L. M.; Huerta-Aguilar, C. A.; Navarrete, E.; Llobet, E.; Thangarasu, P. Enhancement of the CO_2 Sensing/Capture through High Cationic Charge in $M-ZrO_2$ (Li^+, Mg^{2+}, or Co^{3+}): Experimental and Theoretical Studies. *ACS Appl. Mater. Interfaces* **2023**, *15*, 25952.

(57) Tecuapa-Flores, E. D.; Hernandez, J. G.; Roquero-Tejeda, P.; Arenas-Alatorre, J. A.; Thangarasu, P. Rapid Electrochemical Recognition of Trimethoprim in Human Urine Samples Using New Modified Electrodes (CPE/Ag/Au Nps) Analysing Tunable Electrode Properties: Experimental and Theoretical Studies. *Analyst* **2021**, *146*, 7653.

(58) Tecuapa-Flores, E. D.; Palacios-Cabrera, C. B.; Santiago-Cuevas, A. J.; Hernandez, J. G.; Narayanan, J.; Thangarasu, P. Simultaneous Recognition of Dopamine and Uric Acid in Real Samples Through Highly Sensitive New Electrode Fabricated Using ZnO/Carbon Quantum Dots: Bio-Imaging and Theoretical Studies. *Analyst* **2024**, *149*, 108.

(59) Zeng, R.; Qiu, M.; Wan, Q.; Huang, Z.; Liu, X.; Tang, D.; Knopp, D. Smartphone-Based Electrochemical Immunoassay for Point-of-Care Detection of SARS-CoV-2 Nucleocapsid Protein. *Anal. Chem.* **2022**, *94*, 15155.

(60) Lv, S.; Zhang, K.; Zhu, L.; Tang, D.; Niessner, R.; Knopp, D. H_2-Based Electrochemical Biosensor with Pd Nanowires@ZIF-67 Molecular Sieve Bilayered Sensing Interface for Immunoassay. *Anal. Chem.* **2019**, *91*, 12055.